Power Coupling Mechanism Analysis and Improved Decoupling Control for Virtual Synchronous Generator

Tiliang Wen, *Student Member, IEEE*, Donghai Zhu, *Member, IEEE*, Xudong Zou, *Member, IEEE*, Bingchen Jiang, *Student Member, IEEE*, Li Peng, *Member, IEEE*, and Yong Kang, *Senior Member, IEEE*

***Abstract*—A virtual synchronous generator (VSG) control-based grid-connected converter (GCC) is an attractive solution to improve the stability of a more renewable-energy-integrated power system. Unfortunately, the inherent power coupling (i.e., the interaction between the active power loop and the reactive power loop) defect of VSG control severely restricts the power delivery capacity and the grid support capability of the GCC. The virtual inductor is commonly used to reduce coupling, but its decoupling capability is very limited. In addition, the power coupling mechanism and its limiting factors are not clear. For this issue, the nature of power coupling in the VSG system is investigated first. The decoupling capability of the virtual inductor is studied, and the reason for decoupling effectiveness is revealed. It indicates that the effectiveness of decoupling results from the proper voltage compensation, but this kind of positive effect is limited by the *d*-axis voltage drop across the virtual inductor. Then, a *q*-axis voltage-drop-based power decoupling control (QVPDC) is proposed to further reduce the power coupling, which does not consider the *d*-axis voltage drop when applying the virtual inductor. Compared with the virtual-inductor-based decoupling method, the decoupling performance of QVPDC is better, and the computation burden is reduced by half. Finally, the analysis and the proposed method are validated by simulation and experiment.**

***Index Terms*—Grid-connected converter (GCC), power decoupling control, *q*-axis voltage drop, virtual synchronous generator (VSG).**

I. Introduction

NOWADAYS, renewable-energy-based distributed power generation is attracting more and more attention, owing to its environmental friendly feature. Unfortunately, as the interface between distributed power generation and the power system, the grid-connected converter (GCC) cannot provide the adequate inertia support for the grid. Under this circumstance, the more renewable-energy-integrated power system has a risk of instability [1]. Thus, distributed power generation is expected to be involved in the inertial response [2], [3].

To tackle the issue about the lack of inertia, the GCC needs to keep in step with the grid when the grid voltage changes [4]. There are two kinds of methods to cope with this issue: the modified vector current control [5] and the virtual synchronous generator (VSG) control [6]. For the modified vector current control, the differentiation of grid frequency, which is obtained from the phase-locked loop (PLL), is usually used to modify the reference values of current or torque. However, the PLL used in the vector control might induce the instability under the weak grid condition [7], [8]. In addition, the system stability is greatly influenced by the number of paralleled converters [9]. Thus, from the perspective of stability, the authors therein suggest that VSG control is more preferable than the modified vector control. Besides, the modified vector-control-based GCC cannot provide independent voltage support for the loads because of its current source characteristic. On the contrary, without PLL, VSG control enables GCC to emulate the synchronous generator (SG) [10]. By changing the control scheme, the output power can be automatically changed with the grid voltage [11].

Being naturally friendly to the grid, the VSG has attracted much attention, and various research studies have been conducted, such as parameter design [12], frequency restoration [13], impedance analysis [9], [14], damping of resonance [15], [16], variable inertia [17], [18], multioperation-mode analyses [19], model-predictive control [20], and the improvement of transient stability [21], [22]. Although many research studies on VSG control have been conducted, there are still some challenges, among which an important one is the power coupling issue, i.e., any change of the active or reactive power will affect the other. On the one hand, the coupling may degrade the dynamic performance of the power system [23], [24]. On the other hand, because of power coupling, the GCC needs to absorb much reactive power to provide the active power support, which aggravates the reactive power demand of the grid. This severely restricts the active power delivery capability of the GCC [25]. More importantly, the system stable operation may be threatened owing to the limited active power delivery capability [26].

Manuscript received April 1, 2020; revised July 5, 2020; accepted August 11, 2020. Date of publication August 18, 2020; date of current version October 30, 2020. This work was supported in part by the Joint Research Fund in Smart Grid (U1966208) under cooperative agreement between the National Natural Science Foundation of China (NSFC) and State Grid Corporation of China (SGCC), in part by the China Postdoctoral Science Foundation under Grant 2020M672354, and in part by the National Postdoctoral Program for Innovative Talent under Grant BX20180106. Recommended for publication by Associate Editor A. K. Gupta. *(Corresponding author: Donghai Zhu.)*

The authors are with the State Key Laboratory of Advanced Electromagnetic Engineering and Technology and the School of Electrical and Electronic Engineering, Huazhong University of Science and Technology, Wuhan 430074, China (e-mail: tlwen@hust.edu.cn; zhudh@hust.edu.cn; xdzou@mail.hust.edu.cn; chiangbc@hust.edu.cn; pe105@mail.hust.edu.cn; ykang@mail.hust.edu.cn).

Color versions of one or more of the figures in this article are available online at https://ieeexplore.ieee.org.

Digital Object Identifier 10.1109/TPEL.2020.3017254

To improve the decoupling performance of the VSG, various decoupling strategies have been proposed [23], [24], [27]–[34]. Among them, the most widely adopted method is the virtual inductor method [35], owing to its clear physical meaning and easy implementation. It is also the base of other advanced decoupling methods proposed recently. This method employs the virtual inductor to decrease the line impedance ratio R/X and improve the decoupling performance. However, the low-pass filter (LPF) introduced during the virtual inductor implementation leads to the tradeoff between the high-frequency gain attenuation and the emulation accuracy. To avoid the compromise induced by the LPF, the quasi-stationary approximation-based virtual inductor is proposed in [23] and [36] by only considering the fundamental component of the output current. Alternatively, the impedance angle is used in [27]–[30] to apply the rotation transformation, and thus, the impedance can be considered as a pure inductive or resistive. Although the above methods are effective and intuitive, they only focus on the R/X-induced coupling. Actually, the phase difference between the output voltage of the VSG and the grid voltage also has a huge impact on the power coupling [31]. Therefore, some improved decoupling methods are proposed to solve the phase-difference-induced coupling. In [31], the current-compensation-based decoupling method is proposed by modifying the current reference value. In [32], the reference value of torque is modified to reduce the negative effect of the reactive power loop on the active power loop. However, these methods can only solve the phase-difference-induced power coupling.

To simultaneously reduce the power coupling induced by R/X and phase difference, the compensation-matrix-based decoupling method is proposed in [24]. In the method, the reference value of voltage is modified by the special inverse matrix to offset the control-plant-induced coupling. However, this method is complicated and not intuitive. Moreover, the reactive power loop control, another key factor of power coupling, is not considered. In [33], the method combining the virtual impedance and current compensation is proposed to solve the R/X-induced coupling and phase-difference-induced coupling, simultaneously. The method can attain a good decoupling performance by optimizing control parameters. However, the design process depends on the accurate grid frequency; otherwise, the needed $\Delta\theta$ is difficult to obtain. Unfortunately, the accurate information of real-time grid frequency is difficult to obtain, especially in a weak grid. Therefore, it is necessary to further study the power decoupling method in the premise of considering these factors systematically. In [34], the optimal design of the virtual inductor is attained to solve the R/X- and phase-difference-induced power coupling with considering the VSG control. However, the decoupling performance is limited, and the reduction in coupling is about 30%. Furthermore, it is not clear why the decoupling capability of the virtual inductor is limited.

Actually, whatever the factor power coupling is resulted from, it can be attributed to changing the output voltage. From this perspective, various decoupling methods can be attributed to regulating the output voltage of the GCC. For example, Wen *et al.* [34] indicate that the positive effect of the virtual inductor results from the improved output voltage. Therefore, this article systematically studies the power coupling issues of VSG control from the aspect of output voltage compensation. First, the decoupling performance of the classical virtual inductor is analyzed, and the reactive power loop, decoupling strategy, and plant are considered comprehensively. Then, the mechanism of limited decoupling capability of the virtual inductor is analyzed. Afterward, a q-axis voltage-drop-based power decoupling control (QVPDC) method is proposed by neglecting the d-axis voltage drop across the virtual inductor when using the virtual inductor. With the method, the power coupling can be eliminated. Moreover, the proposed method is intuitive and simple, which is conducive to the industrial applications. In short, the main contributions of this article can be summarized as follows.

1) This article points out for the first time the reason for the limited decoupling of the virtual inductor. The physical essence of power coupling is analyzed, which promotes the understanding and development of VSG technology.
2) A novel model of power coupling is established in this article, which can accurately predict the effect of decoupling method, and it also applies to other decoupling methods.
3) The proposed QVPDC method can eliminate the power coupling and improve the grid support capability of the GCC. This method has the advantages of good decoupling performance, simple implementation, clear physical meaning, and small amount of calculation.

The rest of this article is organized as follows. In Section II, the basic principle of VSG control is briefly introduced. In Section III, the mechanism of limited decoupling capability of the virtual inductor is analyzed. In Section IV, the phasor-diagram-based analysis is given to qualitatively explain why the decoupling capability of the virtual inductor is limited. Afterward, a QVPDC method is proposed to further reduce the power coupling. In Section V, the simulation and experimental results are presented to verify the proposed decoupling method. The discussions are given in Section VI. Finally, Section VII concludes this article.

II. Basic Principle of the VSG

A. Structure of the VSG System

The topology and the control block diagram of the VSG are illustrated in Fig. 1. A three-phase voltage-source converter is connected to the ac grid through an LCL filter. L_1, C_f, and L_2 are the inverter-side inductor, filter capacitor, and grid-side inductor, respectively. $\boldsymbol{z_g}$ is the equivalent grid impedance ($\boldsymbol{z_g} = z_g \angle\theta_{zg} = r_g + jx_g$), which contains the line impedance (z_{line}) and L_2. I_1, V_c, I_o, and V_g denote the converter-side current, filter capacitor voltage (output voltage), grid-side current, and grid voltage, respectively. The power decoupling block denotes various decoupling methods, as introduced in Section I. Among them, the virtual-inductor-based decoupling method is the focus of this article.

B. Control of VSG

The detailed control diagram of the VSG is shown in Fig. 2, and the symbols in the figure are explained as follows. P_{ref} and

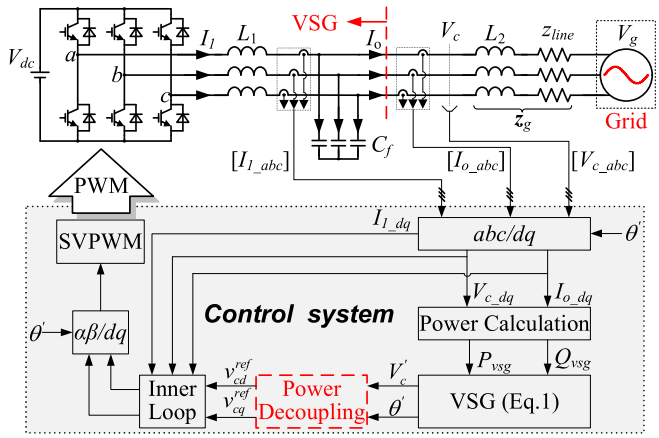

Fig. 1. Generic topology and control block of the VSG.

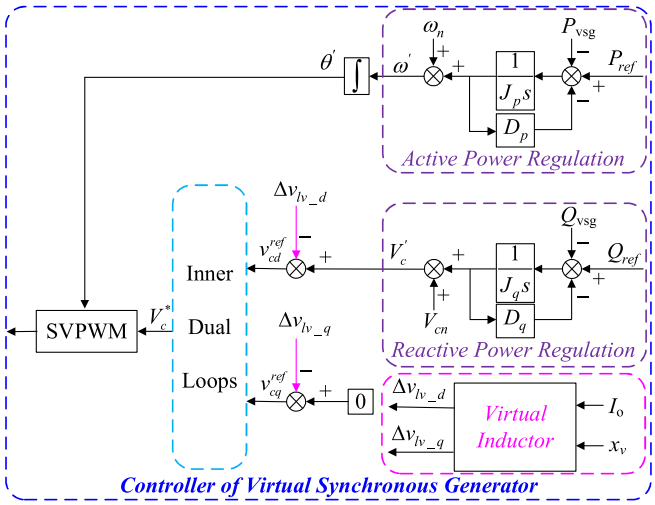

Fig. 2. Control diagram of the VSG.

Q_{ref} are the reference values of the active and reactive power, respectively. P_{vsg} and Q_{vsg} are the output active power and reactive power of the VSG, respectively. D_p and D_q denote the droop coefficients of active and reactive power loops, respectively. J_p and J_q are the virtual inertia coefficients of active and reactive power loops [11], [37], respectively. ω_n and V_{cn} are the rated angular frequency and amplitude of the output voltage, respectively. ω' is the frequency reference value of the output voltage, and θ' denotes its integration. V_c' is the output of the reactive power loop, which is the amplitude reference of output voltage. x_v, Δv_{lv_d}, and Δv_{lv_q} denote the virtual inductance and its d-axis and q-axis voltage drop, respectively.

The mathematical expression of the VSG control can be written as [11]

$$\begin{cases} P_{\text{ref}} - P_{\text{vsg}} - D_p(\omega' - \omega_n) = J_p \dfrac{\mathrm{d}(\omega' - \omega_n)}{\mathrm{d}t} \\ Q_{\text{ref}} - Q_{\text{vsg}} - D_q(V_c' - V_{cn}) = J_q \dfrac{\mathrm{d}(V_c' - V_{cn})}{\mathrm{d}t} \\ \theta' = \displaystyle\int \omega' dt. \end{cases} \tag{1}$$

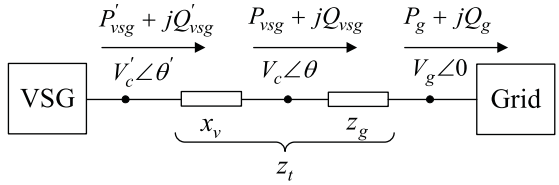

Fig. 3. Equivalent circuit of the grid-connected VSG system with a virtual inductor.

Note that unless explicitly specified in this article, all the variables are expressed in the per-unit (p.u.) values.

Apparently, P_{vsg} and Q_{vsg} are needed to fed into active and reactive power loops, respectively. They can be calculated in the dq frame, as follows:

$$\begin{cases} P_{\text{vsg}} = v_{cd} i_{od} + v_{cq} i_{oq} \\ Q_{\text{vsg}} = v_{cq} i_{od} - v_{cd} i_{oq}. \end{cases} \tag{2}$$

Then, the frequency reference and the magnitude reference are obtained from active and reactive power loops, respectively. After obtaining the voltage reference values, the inner voltage and current loops track the reference values of voltage amplitude and frequency. Apparently, Fig. 1 is equivalent to a voltage-source grid-connected system; thus, the VSG can provide independent voltage support. The output power of the VSG is related to the variations in frequency and amplitude of the grid voltage. As a result, the VSG can contribute to the power system inertial response by automatically adjusting the amplitude and phase of its terminal voltage [11]. Besides, without PLL, the stability concern induced by the PLL is avoided.

When the virtual inductor is employed, the simplified VSG circuit is shown in Fig. 3, where $V_g \angle 0$, $V_c \angle \theta$, and $\boldsymbol{z}_t$ denote the grid voltage, output voltage, and the total impedance, respectively. $P_g + jQ_g$ denotes the absorbed power of the grid. P'_{vsg} and Q'_{vsg} are the virtual active and reactive power, respectively, which are defined for the modeling convenience when the decoupling strategy is applied. Note that the voltage amplitude reference should be adjusted accordingly in this situation. The new reference values can be expressed in dq frame as [23], [34]

$$\begin{cases} v_{cd}^{\text{ref}} = V_c' - \Delta v_{lv\_d} = V_c' + x_v i_{oq} \\ v_{cq}^{\text{ref}} = 0 - \Delta v_{lv\_q} = -x_v i_{\text{od}}. \end{cases} \tag{3}$$

C. Small-Signal Model of the VSG System

According to Fig. 3, the output power of the VSG can be expressed as [38]

$$\begin{cases} P_{\text{vsg}} = \dfrac{V_c^2}{z_g} \cos\theta_{zg} - \dfrac{V_c V_g}{z_g} \cos(\theta_{zg} + \theta) \\ Q_{\text{vsg}} = \dfrac{V_c^2}{z_g} \sin\theta_{zg} - \dfrac{V_c V_g}{z_g} \sin(\theta_{zg} + \theta). \end{cases} \tag{4}$$

Combining Fig. 2 with (4), the small-signal diagram of VSG control can be drawn, as shown in Fig. 4. The control plant model

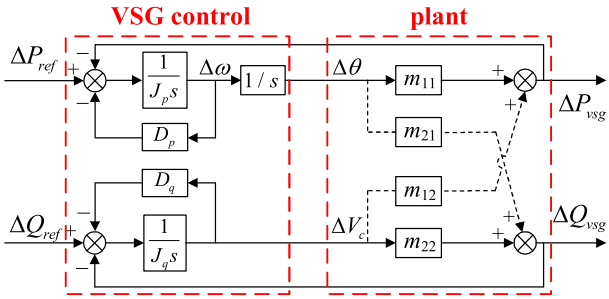

Fig. 4. Small-signal diagram of VSG control.

without decoupling control is shown as

$$\begin{bmatrix}\Delta P_{\text{vsg}}\\ \Delta Q_{\text{vsg}}\end{bmatrix}=\begin{bmatrix}m_{11} & m_{12}\\ m_{21} & m_{22}\end{bmatrix}\begin{bmatrix}\Delta\theta\\ \Delta V_c\end{bmatrix} \tag{5}$$

where m_{11}, m_{12}, m_{21}, and m_{22} are the constants related to the operating point and grid parameters, shown as

$$\begin{cases} m_{11}=\dfrac{V_g}{z_g}V_{c0}\sin\gamma_{c0}\\ m_{12}=\dfrac{2V_{c0}}{z_g}\cos\theta_{zg}-\dfrac{V_g}{z_g}\cos\gamma_{c0}\\ m_{21}=-\dfrac{V_g}{z_g}V_{c0}\left(\cos\gamma_{c0}\right)\\ m_{22}=\dfrac{V_g}{z_g}\left(\dfrac{2V_{c0}}{V_g}\sin\theta_{zg}-\sin\gamma_{c0}\right)\end{cases} \tag{6}$$

where $\gamma_c=\theta_{zg}+\theta$, and subscript 0 denotes the equilibrium point. Note that the calculation of θ is not the focus, and its calculation method can be found in Section III-A.

According to Fig. 4, the open-loop transfer function of active power loop ($G_{p\_\text{open}}(s)$) and reactive power loop ($G_{q\_\text{open}}(s)$) can be easily written as

$$\begin{cases} G_{p\_\text{open}}(s)=\dfrac{m_{11}}{J_p s^2+D_p s}\\ G_{q\_\text{open}}(s)=\dfrac{m_{22}}{J_q s+D_q}.\end{cases} \tag{7}$$

For $r_g=x_g=0.1$ and $Q_{\text{vsg}}=0$, when P_{vsg} changes from 0.5 to 1.0 p.u. (i.e., P_{vsg} =0.5, 0.6, 0.7, 0.8, 0.9, and 1.0 p.u.), the Bode diagrams of active and reactive power loops can be drawn according to (7), as shown in Figs. 5 and 6, respectively. Note that the open-loop transfer function of the reactive power loop is a first-order inertial link, the phase delay is up to 90°, and the phase margin is at least 90°. Thus, both active and reactive power loops are stable. It can be seen that the phase–frequency plot does not change with P_{vsg}, and the magnitude plot hardly changes with P_{vsg}. The study about the effects of operating point on the proposed decoupling method can be found in Section IV-B.

III. Mechanism Analysis of Limited Decoupling Capability of the Virtual Inductor

This section introduces the power coupling model of VSG control with considering the reactive power loop, R/X, phase

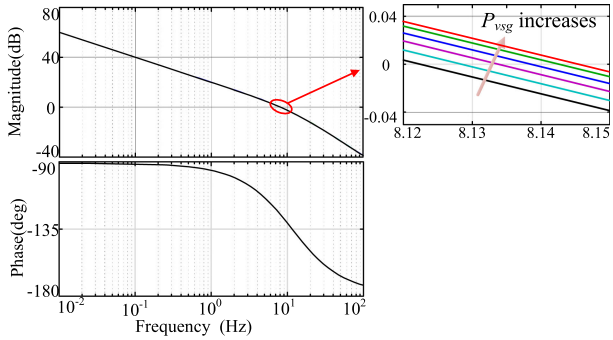

Fig. 5. Bode diagram of the active power loop of the VSG with different operating points.

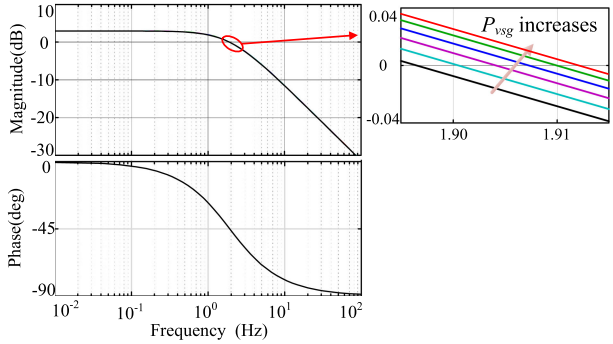

Fig. 6. Bode diagram of the reactive power loop of the VSG with different operating points.

difference, and decoupling control. The role of virtual inductor in reducing the power coupling is studied. Moreover, the relative gain array method is introduced to qualitatively evaluate the decoupling performance of the virtual inductor.

A. Introduction of a Virtual-Inductor-Based Decoupling Method

According to (5), when the grid inductance predominates ($\theta_{zg}\to 90°$) and the phase difference is very small ($\theta\to 0°$), the perturbation of P_{vsg} and Q_{vsg} can be simplified as

$$\begin{cases}\Delta P_{\text{vsg}}=\dfrac{V_{c0}V_g}{z_g}\Delta\theta\\ \Delta Q_{\text{vsg}}=\dfrac{2V_{c0}-V_g}{z_g}\Delta V_c.\end{cases} \tag{8}$$

According to (8), P_{vsg} and Q_{vsg} can be used to adjust θ and V_c, respectively. Thus, the virtual inductor is usually used to pursue the aforesaid predominant inductive grid impedance and improve the decoupling performance [23], [35], [39]. To test the rationality of the hypothesis $\theta\approx 0°$, the expression of θ needs to be calculated.

According to Fig. 3, when the virtual inductor is not considered, $V_c'\angle\theta'=V_c\angle\theta$. In this situation, the phasor diagram of the grid-connected VSG system can be easily drawn, as shown in Fig. 7 (solid lines), where ΔV_{zg} denotes the voltage drop across the z_g, i.e., $\Delta V_{zg}=i_o z_g$. Note that the inner dual loops are considered as a proportional controller with gain 1. When

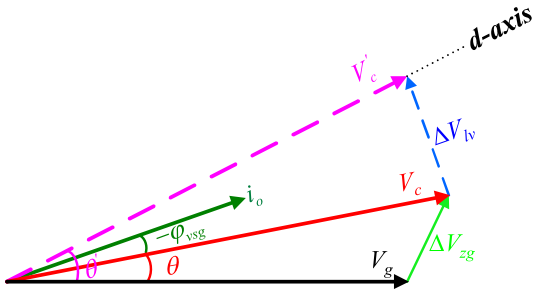

Fig. 7. Phasor diagram of the grid-connected VSG system with the virtual inductor.

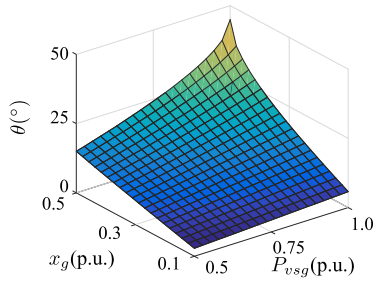

Fig. 8. Surface plot of θ along with x_g and P_{vsg} for $r_g = 0$.

the virtual inductor is used, (3) needs to be considered, and the difference is expressed with dashed lines, as shown in Fig. 7, where ΔV_{lv} denotes the voltage drop across the virtual inductor and φ_{vsg} is the power factor angle. According to Fig. 2, θ' is used for coordinate system transformation. In this article, the location of θ' is chosen as the location of d-axis, as shown in Fig. 7.

According to the phasor diagram shown in Fig. 7, the following expression can be derived with the law of sines:

$$\frac{V_g}{\sin(\theta_{zg}-\varphi_{\text{vsg}})} = \frac{i_o z_g}{\sin\theta} = \frac{V_c}{\sin(180^\circ-\theta-\theta_{zg}+\varphi_{\text{vsg}})} \equiv \lambda \tag{9}$$

where, λ is defined to facilitate the derivation shown below. Considering $V_g = 1.0$ p.u., the apparent power of VSG (S_{vsg}) can be derived with (9), as follows:

$$\begin{aligned} S_{\text{vsg}} &= \frac{P_{\text{vsg}}}{\cos\varphi_{\text{vsg}}} = \frac{1}{z_g}\lambda\sin\theta\cdot\lambda\cdot\sin(180^\circ-\theta-\theta_{z_g}+\varphi_{\text{vsg}}) \\ &= \frac{1}{2Z_g}\frac{\cos(\theta_{z_g}-\varphi_{\text{vsg}})-\cos(\theta_{z_g}-\varphi_{\text{vsg}}+2\theta)}{\sin^2(\theta_{z_g}-\varphi_{\text{vsg}})}. \end{aligned} \tag{10}$$

With (10), θ can be mathematically expressed as

$$\theta = 90^\circ + 0.5\,(\varphi_{\text{vsg}} - \theta_{zg} - \beta) \tag{11}$$

where $\beta = \arccos[2S_{\text{vsg}}z_g\sin^2(\theta_{zg}-\varphi_{\text{vsg}}) - \cos(\varphi_{\text{vsg}}-\theta_{zg})]$.

When $\varphi_{\text{vsg}} = 0^\circ$ and $\theta_{\text{zg}} = 90^\circ$, the surface plot of θ can be drawn according to (11), as shown in Fig. 8. According to Fig. 8, when $P_{\text{vsg}} = 1$ p.u. and $x_g = 0.5$ p.u., θ can be as large as 45°. Thus, the small phase difference assumption used in the derivation of (8) lacks of rationality. Consequently, using a virtual inductor to pursue predominantly inductive impedance also lacks of rationality. In detail, it is difficult to satisfy the two assumptions ($\theta_{zg}\to 90^\circ$ and $\theta\to 0^\circ$) at the same time. Besides, in terms of decoupling, the virtual inductor should not be considered as a real inductor [34].

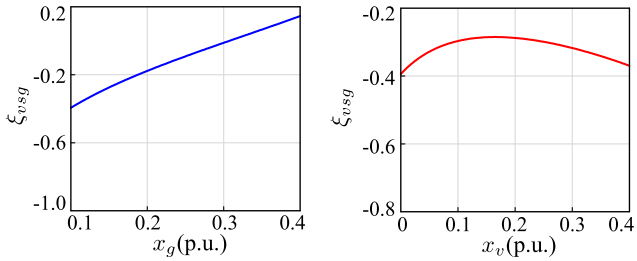

Fig. 9. Plot of ξ_{vsg} with x_g and x_v when $r_g = 0.1$ p.u. (a) ξ_{vsg} with x_g. (b) ξ_{vsg} with x_v ($x_g = 0.1$ p.u.).

B. Power Coupling Model With a Virtual Inductor

According to the small-signal diagram in Fig. 4, the reactive power loop also has a huge impact on power coupling. Thus, the virtual inductor, plant, and VSG control should be considered together when studying the power coupling [34]. Supposing that a disturbance is applied to P_{ref}, the variation of Q_{vsg} can be calculated, as follows [34]:

$$\Delta Q_{\text{vsg}} = \frac{1}{\frac{k_{11}}{k_{21}}\left(1+\frac{k_{22}}{D_q}\right)-\frac{k_{12}}{D_q}}\Delta P_{\text{vsg}} = \xi_{\text{vsg}}\Delta P_{\text{vsg}} \tag{12}$$

where ξ_{vsg} denotes the effect of active power loop on the reactive power loop; the elements k_{11}, k_{12}, k_{21}, and k_{22} are shown as follows:

$$\begin{cases} k_{11} = \dfrac{V_g}{z_t}V'_{c0}\sin\gamma'_{c0} \\ k_{12} = \dfrac{2V'_{c0}}{z_t}\cos\theta_{zt} - \dfrac{V_g}{z_t}\cos\gamma'_{c0} \\ k_{21} = -\dfrac{V_g}{z_t}V'_{c0}\left(\cos\gamma'_{c0} + \dfrac{2x_v}{z_t}\sin\theta'_0\right) \\ k_{22} = \dfrac{V_g}{z_t}\left(\dfrac{2V'_{c0}}{V_g}\sin\theta_{zt} - \dfrac{2x_vV'_{c0}}{z_tV_g} + \dfrac{2x_v}{z_t}\cos\theta'_0 - \sin\gamma'_{c0}\right) \end{cases} \tag{13}$$

where $\gamma'_c = \theta_{zt}+\theta'$, and θ' can be calculated according to (11).

Equation (12) is a general description of power coupling with a virtual inductor and can be simplified into various forms. When x_v in (12) is zero, the plot of ξ_{vsg} along with x_g can be drawn, as shown in Fig. 9(a). According to the figure, ξ_{vsg} increases monotonously with x_g, and when x_g is larger than 0.3 p.u., $\xi_{\text{vsg}} > 0$. When x_v is taken into account, the plot of ξ_{vsg} along with x_v is shown in Fig. 9(b). Obviously, there is no positive correlation between ξ_{vsg} and x_v, and when $x_v > 0.17$ p.u., the larger x_v leads to reduced decoupling performance. Thus, there is a huge difference between the virtual inductor and the real inductor.

C. Limited Power Decoupling Capability of the Virtual Inductor

To evaluate the coupling of a multi-input multi-output system, the relative gain array method [40] is usually adopted. Suppose the input variables of the system are $[u_1, u_2, \ldots, u_n]$, and the output variables are $[y_1, y_2, \ldots, y_n]$; the first and second amplification factors are

$$\begin{cases} p_{ij} = \left.\dfrac{\partial y_i}{\partial u_j}\right|_{u_k=\text{const},k\neq j} \\ q_{ij} = \left.\dfrac{\partial y_i}{\partial u_j}\right|_{y_k=\text{const},k\neq i} \end{cases} \tag{14}$$

where "const" means constant. For dual-input and dual-output systems of the VSG shown in Fig. 4, the relative gain array is a second-order square matrix and can be calculated with (14), as follows:

$$\rho = \begin{bmatrix} \rho_{11} & \rho_{12} \\ \rho_{21} & \rho_{22} \end{bmatrix} \tag{15}$$

where $\rho_{ij} = \frac{p_{ij}}{q_{ij}}$, which denotes the relative coupling gain of y_i to u_j. Note that the coupling is related to VSG control, decoupling strategy, and control plant; the relative gain array is related to D_q, virtual inductor, and plant. However, the calculation of $p_{11}, p_{21}, q_{11},$ and q_{21} is relatively difficult because of the integration "$\int$" in the active power loop. Besides, the math expression of plant changes with the operating point, i.e., the parameters $k_{11}, k_{12}, k_{21},$ and k_{22} change with P_{vsg} and Q_{vsg}. Thus, to make it easy, the partial derivative operation shown in (14) is finished by a numerical method. In detail, the curves of P_{vsg} and Q_{vsg} are calculated with (12), and the needed partial derivative can be attained. The properties of matrix ρ are mathematically expressed as

$$\rho_{ij} = \rho_{ji}, \quad \sum_{j=1}^{2} \rho_{ij} = 1, \quad \sum_{i=1}^{2} \rho_{ij} = 1. \tag{16}$$

Note that the closer ρ_{ii} is to 1, the better the decoupling performance. Considering $\rho_{11}+\rho_{12}=1$ [see (16)], it can also be said that the closer ρ_{12} is to 0, the lower power coupling. In conclusion, the relative gain array of VSG control can be calculated according to (1), (3), (12), (14), and (15).

The plots of ρ_{12} with P_{vsg} under different virtual inductors are shown in Fig. 10. When $x_v=0$, ρ_{12} is far away from zero, which means that the power coupling is serious in this situation. When $x_v=0.17$ p.u., ρ_{12} is closer to zero and the decoupling performance is the best. However, when x_v continues to increase, the decoupling performance is deteriorated. Furthermore, ρ_{12} cannot be reduced to 0; thus, the power coupling cannot be eliminated. Once the outputs of the voltage control loop are saturated due to the capacity limit, the instability issue may occur [26].

Note that the output reactive power is significantly influenced by the voltage output [41]. The plots of V_c and the output voltage of ideally decoupled case (V_{c_ide}) are drawn according to (12), as shown in Fig. 11. The comparison between Fig. 11(a) and (b) indicates that the virtual inductor cannot reduce the gap between

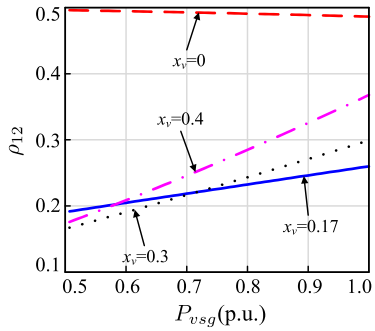

Fig. 10. Plots of ρ_{12} for virtual inductor decoupling with different x_v.

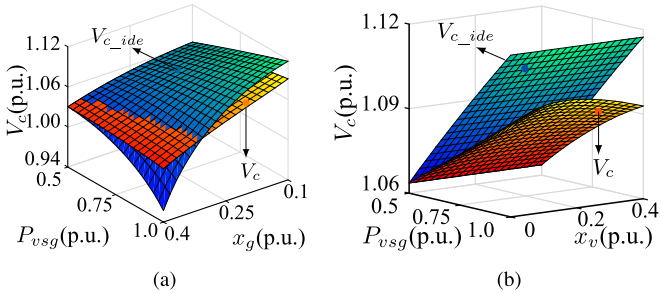

Fig. 11. Gap between V_c and the desired output voltage (V_{c_ide}) for $r_g = 0.1$ p.u. (a) Surface graph of $V_c(P_{\text{vsg}}, x_g)$. (b) Surface graph of $V_c(P_{\text{vsg}}, x_v)$.

V_{c_ide} and V_c to 0. The comparison between Figs. 9 and 11 indicates that the best decoupling performance is achieved when the voltage gap is minimum, and the positive effect of virtual inductor results from the reduced voltage gap. Therefore, larger voltage compensation is needed to further reduce coupling in this situation.

In conclusion, the virtual inductor has limited capability to improve the decoupling performance, owing to the limited voltage compensation capability. Therefore, if the limiting factor of decoupling capability can be identified and avoided, the power decoupling capability of the virtual inductor will be improved. Based on this idea, the QVPDC method is proposed in the next section.

IV. Proposed QVPDC Method

A. Basic Principle

As expressed in Section III, the limited voltage compensation capability of the virtual inductor hinders the further reduction in coupling. Thus, it is important to identify the limiting factor of the virtual inductor. Combining (3) with Fig. 7, the relation between $V_c' \angle\theta'$ and $V_c \angle\theta$ can be written as

$$\begin{cases} v_{cd} = V_c' - \Delta v_{lv\_d} = V_c' + i_o \sin(\theta - \varphi_{\text{vsg}} - \theta')x_v \\ v_{cq} = 0 - \Delta v_{lv\_q} = 0 - i_o \cos(\theta - \varphi_{\text{vsg}} - \theta')x_v. \end{cases} \tag{17}$$

The voltage compensation provided by the virtual inductor can be qualitatively analyzed with Fig. 7 and (17). At first, $Q_{\text{vsg}} = 0$, and $\boldsymbol{i_o}$ is in-phase with d-axis, which is given by the active power loop and in-phase with $\boldsymbol{V_c'}$. Due to the use of virtual inductor, the phase of $\boldsymbol{V_c}$ and $\boldsymbol{i_o}$ at the steady-state

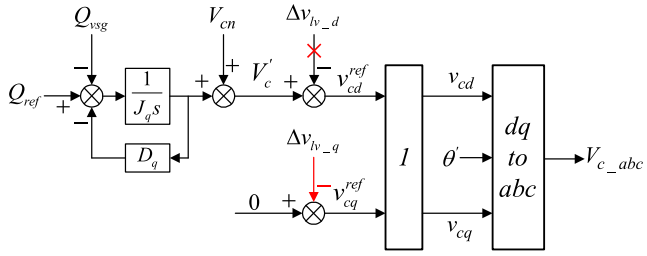

Fig. 12. Decoupling scheme with the proposed QVPDC method.

lag behind the d-axis. The relatively small x_v will result in smaller v_{cd} ($v_{cd} < V_c'$) and v_{cq} (note that v_{cq} is negative). Considering that $|\theta' - \theta|$ is small in this situation, $|\Delta v_{lv\_d}|$ is relatively small, $V_c > V_c'$, and the coupling can be reduced. However, larger voltage increment is not always accessible. As x_v increases, the negative effect of Δv_{lv_d} becomes more and more significant, and V_c might decrease for an excessively large x_v. Thus, the positive d-axis voltage drop across x_v hinders the further reduction in the coupling.

The above analysis can be roughly expressed mathematically as follows. The voltage amplitude without virtual inductor is assumed to be 1 p.u. The voltage output after the use of the virtual inductor can be expressed as $(1 - \Delta v_{lv\_d}) + j\Delta v_{lv\_q}$. The square of voltage increment induced by the virtual inductor is about $(-2\Delta v_{lv\_d} + \Delta v_{lv\_d}^2 + \Delta v_{lv\_q}^2)$. Because $|\Delta v_{lv\_d}|$ is usually smaller than 1, $-2\Delta v_{lv\_d}$ will lead the growth trend when x_v continues to increase. Thus, the square of voltage increment induced by the virtual inductor is limited by Δv_{lv_d}. That is, the d-axis voltage drop across the virtual inductor might be the limiting factor of decoupling capability.

To improve the decoupling capability, one intuitive idea is to remove the constraint of Δv_{lv_d}. Thus, the QVPDC method is proposed in this article, which does not consider the d-axis voltage drop (shown with "$\times$") when implementing a virtual inductor, as shown in Fig. 12. Apparently, a significant advantage of QVPDC over the virtual-inductor-based decoupling method is that the amount of computation is reduced by half.

B. Implementation

The discussion in Section IV-A points out the direction of reducing power coupling. Thus, the detailed coupling model of QVPDC is needed to design the parameter and evaluate the decoupling performance.

According to Fig. 4 and [34], the effect of decoupling control is equivalent to changing the control plant. Thus, a crucial step is to figure out the model of equivalent plant, i.e., the relationship between $P_{\text{vsg}}, Q_{\text{vsg}}$, and $V_c' \angle\theta'$. When the decoupling control is not used, the plant model is shown in (5). When the virtual-inductor-based decoupling method is used, the equivalent plant can be expressed as [34]

$$\begin{bmatrix} \Delta P_{\text{vsg}} \\ \Delta Q_{\text{vsg}} \end{bmatrix} = \begin{bmatrix} k_{11} & k_{12} \\ k_{21} & k_{22} \end{bmatrix} \begin{bmatrix} \Delta\theta' \\ \Delta V_c' \end{bmatrix} \tag{18}$$

where the parameters k_{11}, k_{12}, k_{21}, and k_{22} are the same as those shown in Section III-B. However, for the QVPDC method, it is hard to write this expression as simple as that expressed in [34]. This is because the power loss characteristics are different in this situation.

To give the small-signal model of the equivalent model, it is crucial to give the expressions of P_{vsg} and Q_{vsg}. This issue can be broken down into the calculation of output voltage (v_{cd}, v_{cq}) and output current (i_{od}, i_{oq}). According to Fig. 12, v_{cd} and v_{cq} can be expressed as

$$v_{cd} = V_c', \quad v_{cq} = 0 - \Delta v_{lv\_q} = -\zeta_v i_{od} \tag{19}$$

where ζ_v can be considered as the particular virtual inductor used in the proposed QVPDC method to distinguish from the usual virtual inductor.

Clearly, the expressions of the output currents i_{od} and i_{oq} are needed to calculate the output power of the VSG, and this can be attained with the phasor diagram. As shown in Fig. 7, $\boldsymbol{V_c}$ is related to $\boldsymbol{V_g}$ and can be expressed as

$$\begin{cases} v_{cd} = V_g \cos\theta' + r_g i_{od} - x_g i_{oq} \\ v_{cq} = -V_g \sin\theta' + r_g i_{oq} + x_g i_{od}. \end{cases} \tag{20}$$

Then, substituting (20) into (19), yields

$$\begin{cases} i_{od} = \lambda_{d1} \cos(\theta_{zg} + \theta') + \lambda_{d2} V_c' \\ i_{oq} = \lambda_{q1} \sin(\theta_{zt} + \theta') + \lambda_{q2} V_c' \end{cases} \tag{21}$$

where

$$\begin{cases} \lambda_{d1} = \dfrac{-z_g V_g}{z_g^2 + x_g\zeta_v}, \ \lambda_{d2} = \dfrac{r_g}{z_g^2 + x_g\zeta_v} \\ \lambda_{q1} = \dfrac{z_t V_g}{z_g^2 + x_g\zeta_v}, \ \lambda_{q2} = \dfrac{-x_t}{z_g^2 + x_g\zeta_v}. \end{cases} \tag{22}$$

According to (2), (19), and (21), the output power can be calculated as

$$\begin{cases} P_{\text{vsg}} = V_c' [\lambda_{d1} \cos(\theta_{zg} + \theta') + \lambda_{d2} V_c'] \\ \qquad -\zeta_v [\lambda_{d1} \cos(\theta_{zg} + \theta') + \lambda_{d2} V_c'][\lambda_{q1} \sin(\theta_{zt} + \theta') \\ \qquad + \lambda_{q2} V_c'] \\ Q_{\text{vsg}} = -\zeta_v [\lambda_{d1} \cos(\theta_{zg} + \theta') + \lambda_{d2} V_c']^2 \\ \qquad - V_c' [\lambda_{q1} \sin(\theta_{zt} + \theta') + \lambda_{q2} V_c']. \end{cases} \tag{23}$$

Linearizing (23) around the equilibrium point, the needed mathematical model of equivalent plant using QVPDC can be derived as

$$\begin{bmatrix} \Delta P_{\text{vsg}} \\ \Delta Q_{\text{vsg}} \end{bmatrix} = \boldsymbol{\mathcal{A}} \begin{bmatrix} \triangle\theta' \\ \triangle V_c' \end{bmatrix} = \begin{bmatrix} A_{11} & A_{12} \\ A_{21} & A_{22} \end{bmatrix} \begin{bmatrix} \triangle\theta' \\ \triangle V_c' \end{bmatrix} \tag{24}$$

where

$$\begin{cases} A_{11} = (\zeta_v\lambda_{q2} - 1)V'_{c0}\lambda_{d1}\sin(\theta_{zg} + \theta'_0) \\ \qquad - \zeta_v\lambda_{d1}\lambda_{q1}\cos(\theta_{zg} + \theta_{zt} + 2\theta'_0) \\ \qquad - \zeta_v V'_{c0}\lambda_{d2}\lambda_{q1}\cos(\theta_{zt} + \theta'_0) \\ A_{12} = \lambda_{d1}(1 - \zeta_v\lambda_{q2})\cos(\theta_{zg} + \theta'_0) \\ \qquad + 2\lambda_{d2}V'_{c0}(1 - \zeta_v\lambda_{q2}) - \zeta_v\lambda_{d2}\lambda_{q1}\sin(\theta_{zt} + \theta'_0) \\ A_{21} = 2\zeta_v[\lambda_{d1}\cos(\theta_{zg} + \theta'_0) + \lambda_{d2}V'_{c0}]\lambda_{d1}\sin(\theta_{zg} + \theta'_0) \\ \qquad - V'_{c0}\lambda_{q1}\cos(\theta_{zt} + \theta'_0) \\ A_{22} = -2\zeta_v[\lambda_{d1}\cos(\theta_{zg} + \theta'_0) + \lambda_{d2}V'_{c0}]\lambda_{d2} \\ \qquad - \lambda_{q1}\sin(\theta_{zt} + \theta') - 2\lambda_{q2}V'_{c0}. \end{cases} \tag{25}$$

Clearly, according to (25), the parameters of $\boldsymbol{\mathcal{A}}$ are closely related to the operating points. Thus, the effect of operating point is considered in the equivalent control plant, and the change of operating point has little effect on the decoupling method proposed in this article.

According to Fig. 7, v_{cq} and i_{od} can be mathematically expressed as

$$v_{cq} = V_c\sin(\theta - \theta'), \quad i_{od} = i_o\cos(\theta - \varphi_{\text{vsg}} - \theta'). \tag{26}$$

According to (19), $v_{cq} + \zeta_v i_{od} = 0$. Thus, the needed θ' can be calculated with (26), as follows:

$$\theta' = \arctan\frac{V_c\sin\theta + \zeta_v i_o\cos(\theta - \varphi_{\text{vsg}})}{V_c\cos\theta - \zeta_v i_o\sin(\theta - \varphi_{\text{vsg}})}. \tag{27}$$

The expression of ξ_{vsg} for the QVPDC method can be derived by combining (1), (24), and (27), as follows:

$$\Delta Q_{\text{vsg}} = \frac{1}{\frac{A_{11}}{A_{21}}\left(1 + \frac{A_{22}}{D_q}\right) - \frac{A_{12}}{D_q}}\Delta P_{\text{vsg}} = \xi_{\text{vsg}}\Delta P_{\text{vsg}}. \tag{28}$$

According to (28), power coupling is closely related to D_q. Thus, the control of VSG itself also has important effect on power coupling. On the contrary, power coupling of the traditional SG is only related to the equivalent impedance and operating points. Thus, power coupling in the SG does not include the influence of control strategy, and the coupling model in the SG is equivalent to the control plant model in (24).

C. Power Decoupling Performance Analysis

To verify the effectiveness of the qualitative analysis in Section IV-A, the theoretical decoupling performance of QVPDC is needed. Similar to the process in Section III, the qualitative and quantitative decoupling performances of the proposed method are explored in this section.

For the qualitative decoupling performance evaluation, the relative gain array using the QVPDC strategy is calculated. According to (1), (14), (15), (19), and (28), ρ_{12} can be calculated, as shown in Fig. 13. Note that the closer ρ_{12} is to 0, the lower the power coupling. Apparently, the curve ($\zeta_v = 0.4$) is very close

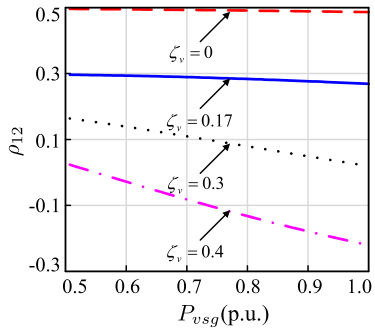

Fig. 13. Plots of ρ_{12} for QVPDC with different ζ_v.

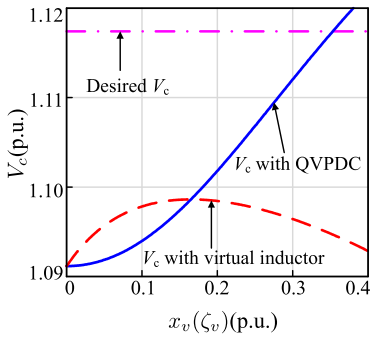

Fig. 14. Gap between V_c and desired output voltage.

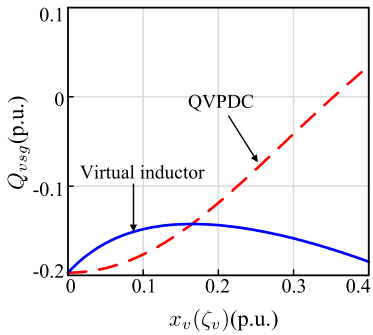

Fig. 15. Theoretical Q_{vsg} when P_{vsg} changes from 0.5 to 1.0 p.u.

to zero. Thus, compared with the conventional virtual-inductor-based decoupling method shown in Fig. 10, the proposed method can achieve better decoupling performance.

Since the purpose of the proposed method is to improve the voltage compensation capability, the curve of V_c with different ζ_v is drawn, as shown in Fig. 14. Note that the horizontal line denotes the desired V_c, which indicates that the coupling is eliminated when the output voltage approaches this value. This horizontal line can be used to check whether the proposed method has the ability to eliminate coupling. Apparently, for the virtual-inductor-based decoupling method, the desirable V_c is not accessible. On the contrary, with the QVPDC method, V_c can reach the horizontal line when $\zeta_v = 0.35$ p.u. Because of larger voltage compensation capability, the QVPDC strategy enables the elimination of coupling.

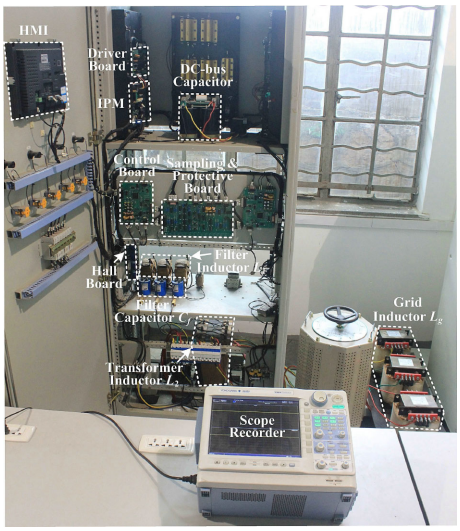

Fig. 16. Photograph of the 7.0-kW VSG prototype.

The theoretical results of Q_{vsg} are shown in Fig. 15. For the virtual-inductor-based decoupling method, the best decoupling performance ($\Delta Q_{\text{vsg}} \approx -0.14$ p.u.) is achieved when $x_v = 0.17$ p.u. An excessively large x_v even deteriorates the decoupling performance. Besides, only 30% reduction in the power coupling can be acquired in this situation. On the contrary, Q_{vsg} can be reduced to 0 with the proposed QVPDC method (when $\zeta_v \approx 0.35$). Thus, compared with the virtual-inductor-based decoupling method, the proposed QVPDC method can eliminate the power coupling.

In conclusion, the results of relative gain array, voltage compensation, and Q_{vsg} all indicate that QVPDC can eliminate the coupling effectively.

V. Simulation and Experiment Verification

To verify the effectiveness of the theoretical analysis, a simulation model is built in MATLAB/Simulink. P_{ref} changes from 0.5 to 1.0 p.u., keeping $Q_{\text{vsg}}^{\text{ref}} = 0$, and the power response curves are acquired. Furthermore, the experimental test of a 7.0-kW VSG prototype is conducted, and its photograph is shown in Fig. 16. The system parameters are listed in Table I. P_{vsg} and Q_{vsg} are output by an 8-bit DA chip (MAX548 A), and all waveforms are acquired by a 16-channel scope recorder (YOKOGAWA DL850E).

A. Simulation Results

For the virtual-inductor-based decoupling method, the simulation results of P_{vsg}, Q_{vsg}, P_g, and Q_g for different virtual inductors are shown in Fig. 17. According to Fig. 17(b), when $x_v = 0.17$ p.u., Q_{vsg} in the steady state increases from -0.2 to -0.14 p.u. When x_v increases to 0.3 p.u., $Q_{\text{vsg}} = -0.16$ p.u., and the decoupling performance is degraded. When x_v continues to increase, such as $x_v = 0.4$ p.u., the decoupling performance keeps decreasing, which is close to the situation of no decoupling strategy. Apparently, a suitable virtual inductor can reduce coupling, but the decoupling performance is limited. Besides,

TABLE I
Parameters of the VSG Control System

Parameter	Symbol	Value
Base value of line voltage	V_{base}	380 V
Base value of power	S_{base}	7.0 kVA
Base value of frequency	f_{base}	50 Hz
Sampling frequency	f_s	200 p.u.
Converter-side inductor of LCL filter	L_1	0.086 p.u.
Capacitor of LCL filter	C_f	0.050 p.u.
Grid-side inductor of LCL filter	L_2	0.023 p.u.
Inductance of the line	L_{line}	0.077 p.u.
Resistance of the line	r_{line}	0.1 p.u.
Rated voltage of grid	V_g	1.0 p.u.
Droop coefficient of reactive power loop	D_q	10 p.u.
Droop coefficient of active power loop	D_p	100 p.u.
Inertia coefficient of reactive power loop	J_q	0.830 p.u.
Inertia coefficient of active power loop	J_p	0.690 p.u.

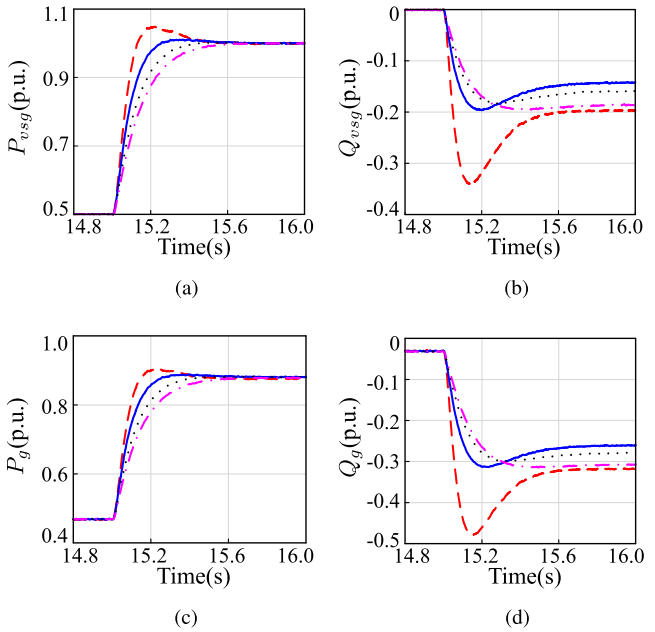

Fig. 17. Simulation results of P_{vsg}, Q_{vsg}, P_g, and Q_g for the virtual-inductor-based decoupling method under different x_v when $r_g = x_g = 0.1$ p.u. - - - -: $x_v = 0$ p.u.; ——: $x_v = 0.17$ p.u.; .....: $x_v = 0.3$ p.u.; -·-·-: $x_v = 0.4$ p.u. (a) P_{vsg}. (b) Q_{vsg}. (c) P_g. (d) Q_g.

compared with the theoretical result shown in Fig. 9(a), it is clear that there is a huge difference between the virtual and real inductors. For example, when $x_g = 0.4$ p.u., the output reactive power is 0.18 p.u. However, when $x_v = 0.3$ p.u., the output reactive power is -0.16 p.u. Power coupling not only affects the power transmission capacity of the GCC, but also aggravates the reactive power demand of the grid. For example, when $x_v = 0.17$ p.u., the grid is forced to output 0.26 p.u. reactive power, as shown in Fig. 17(d). From the above analysis, it is clear that the simulation results about virtual inductor are well consistent with the corresponding theoretical results in Fig. 15.

When P_{ref} changes from 0.5 to 1.0. p.u., the simulation results of power response for the QVPDC method are shown

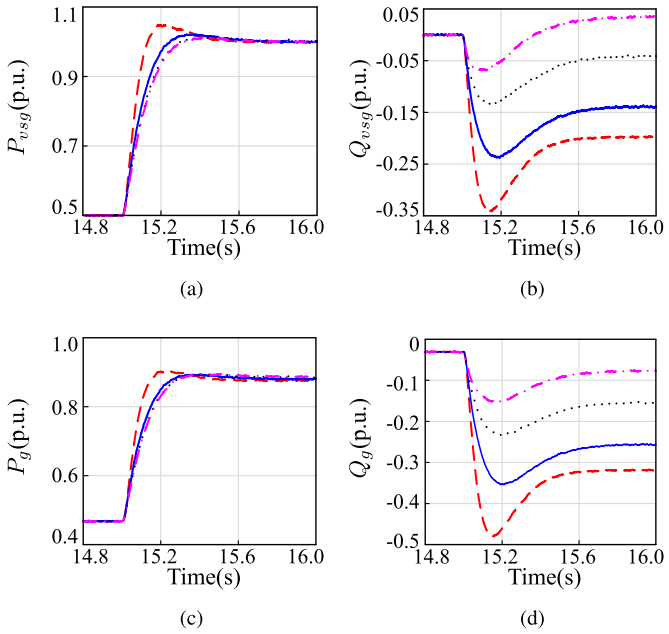

Fig. 18. Simulation results of P_{vsg}, Q_{vsg}, P_g, and Q_g for the QVPDC strategy under different ζ_v when $r_g = x_g = 0.1$ p.u. - - - -: $\zeta_v = 0$ p.u.; ——: $\zeta_v = 0.17$ p.u.; .....: $\zeta_v = 0.3$ p.u.; _ . _ .: $\zeta_v = 0.4$ p.u. (a) P_{vsg}. (b) Q_{vsg}. (c) P_g. (d) Q_g.

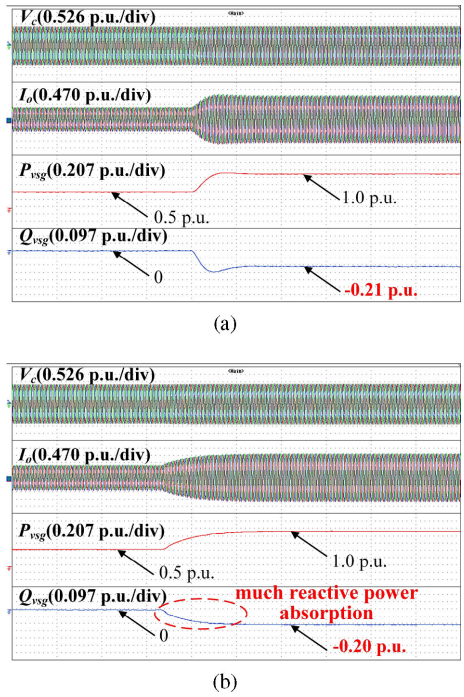

Fig. 19. Experimental results of P_{vsg} and Q_{vsg} when P_{ref} changes from 0.5 to 1.0 p.u. and $r_g = x_g = 0.1$ p.u. (a) Without virtual inductor ($x_v = 0$ p.u.). (b) Classical virtual inductor decoupling method with $x_v = 0.40$ p.u..

in Fig. 18. When the decoupling strategy is not used ($\zeta_v = 0$), $Q_{\text{vsg}} = -0.2$ p.u. When $\zeta_v = 0.17$ p.u., Q_{vsg} increases from -0.2 to -0.14 p.u., which reaches the best decoupling performance of the virtual inductor. When $\zeta_v = 0.3$ p.u., Q_{vsg} reaches -0.04 p.u., and the power coupling of the VSG system has been reduced to a very low level. Furthermore, the reactive power demand of grid reduces from 0.32 to 0.16 p.u. in this situation, as shown in Fig. 18(d). When $\zeta_v = 0.4$ p.u., $Q_{\text{vsg}} = 0.03$ p.u., which means that the system has positive output reactive power at this time. Correspondingly, the reactive power shortage of grid keeps decreasing, as shown in Fig. 18(d). From the comparison between Figs. 15 and 18, it can be seen that the simulation results about QVPDC agree well with theoretical results. Compared with the virtual-inductor-based decoupling method, the proposed QVPDC strategy can eliminate the power coupling.

B. Experimental Results of the Classical Virtual Inductor Decoupling Method

For the classical virtual-inductor-based decoupling method [23], [35], [39], a predominantly inductive impedance is pursued with virtual inductor. Thus, a relatively large virtual inductor ($x_v = 0.4$ p.u. and $X/R = 5$) is selected to verify the decoupling performance, as shown in Fig. 19. Note that the experiment without virtual inductor is also carried out for comparison, as shown in Fig. 19(a). According to Fig. 19(a), when the virtual inductor is not used, $\Delta Q_{\text{vsg}} = -0.21$ p.u., which means that the VSG needs to absorb 0.21 p.u. reactive power. However, according to Fig. 19(b), when $x_v = 0.4$ p.u., $\Delta Q_{\text{vsg}} = -0.2$ p.u., and the improvement of decoupling performance is little. Thus, the predominant inductive impedance pursued by the virtual inductor is inappropriate for decoupling.

TABLE II
THEORETICAL, SIMULATION, AND EXPERIMENTAL ΔQ_{vsg} FOR DIFFERENT VIRTUAL INDUCTORS

ΔQ_{vsg} (p.u.) \ x_v (p.u.)	0.0	0.17	0.30	0.40
theoretical results	−0.20	−0.14	−0.16	−0.18
simulation results	−0.20	−0.14	−0.16	−0.19
experimental results	−0.21	−0.15	−0.18	−0.20

C. Experimental Results of the Optimal Virtual Inductor Decoupling Method

To improve the decoupling effect of virtual inductor as much as possible, the optimal design of the virtual inductor is studied in [34]. According to the optimal design introduced therein, the optimal virtual inductor is about 0.17 p.u. To verify the best decoupling performance of the virtual inductor in this situation, the corresponding experimental curves of P_{vsg} and Q_{vsg} are shown in Fig. 20(a). Note that the results for $x_v = 0.3$ p.u. are also carried out for comparison, as shown in Fig. 20(b). Apparently, when $x_v = 0.17$ p.u., $\Delta Q_{\text{vsg}} = -0.15$ p.u., and when $x_v = 0.3$ p.u., $\Delta Q_{\text{vsg}} = -0.18$ p.u. Compared with Fig. 19(b), it is clear that the optimal decoupling performance is achieved at the appropriate inductor, not the maximum inductor.

For the convenience of comparison, theoretical, simulation, and experimental results for different virtual inductors are summarized in Table II. Apparently, experimental, simulation, and theoretical results are well consistent. However, even though the

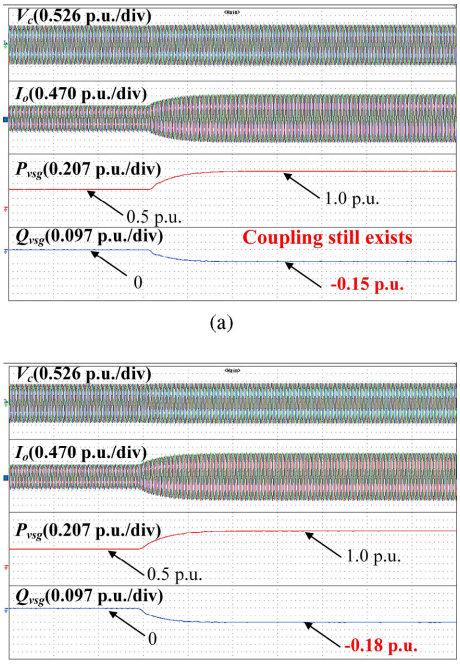

Fig. 20. Experimental results of P_{vsg} and Q_{vsg} when P_{ref} changes from 0.5 to 1.0 p.u. and $r_g = x_g = 0.1$ p.u. (a) Optimal virtual inductor decoupling method ($x_v = 0.17$ p.u.). (b) Classical virtual inductor decoupling method with $x_v = 0.30$ p.u.

TABLE III
THEORETICAL, SIMULATION, AND EXPERIMENTAL RESULTS OF ΔQ_{vsg} FOR THE PROPOSED QVPDC METHOD

ΔQ_{vsg}(p.u.) \ ζ_v (p.u.)	0.0	0.17	0.30	0.40
theoretical results	−0.20	−0.14	−0.04	0.03
simulation results	−0.20	−0.14	−0.04	0.04
experimental results	−0.21	−0.13	−0.02	0.06

optimal virtual inductor is used, the improvement of ΔQ_{vsg} is about 30%. Therefore, the decoupling capability of the virtual inductor is limited.

D. Experimental Results of the QVPDC Method

The experimental results of the QVPDC method are shown in Fig. 21. Similarly, the theoretical (see Fig. 15), simulation (see Fig. 18), and experimental results are also shown in Table III for the convenience of comparison.

As shown in Table III, when $\zeta_v = 0.17$ p.u., the experimental ΔQ_{vsg} is -0.13 p.u., which is consistent with the theoretical value (-0.14 p.u.). When $\zeta_v = 0.3$ p.u., the experimental ΔQ_{vsg} is -0.02 p.u., and the corresponding theoretical value is about -0.04 p.u. Under this situation, the active power support of GCC has little effect on the output reactive power. On the contrary, for the optimal virtual-inductor-based decoupling method, the GCC needs to absorb 0.15-p.u. reactive power. As a result, the reactive power shortage of the grid is aggravated. More importantly, the GCC needs more capacity to fulfill the active power transmission. If the capacity is insufficient, the current

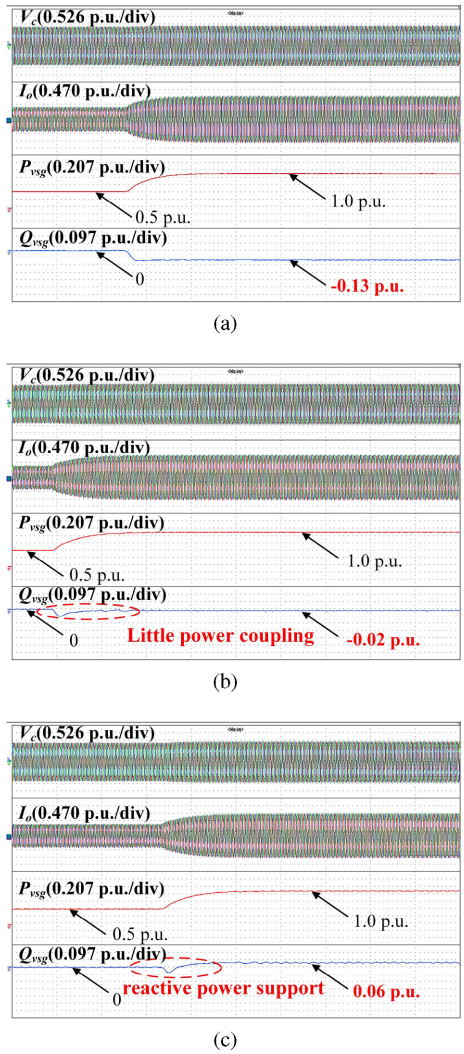

Fig. 21. Experimental results of P_{vsg} and Q_{vsg} when P_{ref} changes from 0.5 to 1.0 p.u. and $r_g = x_g = 0.1$ p.u. (a) QVPDC method with $\zeta_v = 0.17$. (b) QVPDC method with $\zeta_v = 0.30$. (c) QVPDC method with $\zeta_v = 0.40$.

loop will be saturated, which will threaten the system stable operation [26].

When $\zeta_v = 0.4$ p.u., the experimental ΔQ_{vsg} is 0.06 p.u. (see Table III), and the corresponding theoretical value is about 0.04 p.u. The positive output reactive power can relieve the reactive power necessity of grid. Besides, this is conducive to the active power transfer capability of the GCC [25] and the stability of the system [26]. In conclusion, the model shown in (28) can accurately describe the coupling behavior of the system, and the proposed QVPDC decoupling method can eliminate the power coupling of VSG control. For convenience, the comparison among various decoupling methods is summarized, as shown in Table IV.

VI. DISCUSSION

A. Comparison Between VSG and Modified Vector Control

For the power-electronics-based grid-connected system, to emulate the inertial characteristic of the SG, the power

TABLE IV
COMPARISON AMONG VARIOUS DECOUPLING METHODS

Decoupling methods	Considered factors			Evaluation indicators			
	R/X	θ	VSG control	Obvious physical meaning	Accurate coupling description	Easy implementation	Decoupling performance
[23], [27]–[30]	$\surd$	$\times$	$\times$	High	Low	High	Low
[31], [32]	$\times$	$\surd$	$\times$	Low	Moderate	Low	Moderate
[24], [33]	$\surd$	$\surd$	$\times$	Low	Moderate	Low	Moderate
[34]	$\surd$	$\surd$	$\surd$	High	High	High	Moderate
Proposed QVPDC	$\surd$	$\surd$	$\surd$	High	High	High	High

Note: the symbol $\surd$ denotes the positive property, and $\times$ denotes the negative property.

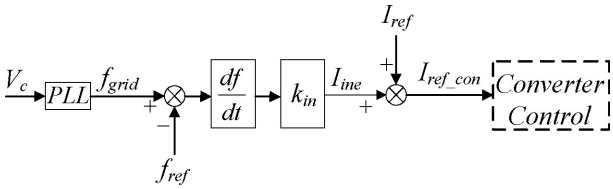

Fig. 22. Modified vector control with of inertia emulation.

unbalance should be alleviated timely. Thus, the change rate of grid frequency f_{grid} is used to determine how much power needs to be compensated, as shown in Fig. 22, where I_{ref} denotes the current reference value of the converter without inertia emulation. k_{in} is the controller constant, which is related to the emulated inertia. I_{ine} is the correction of current reference value given by inertia emulation, and the detailed expression is

$$I_{\text{ine}} = k_{\text{in}} \frac{d(f_{\text{grid}} - f_{\text{ref}})}{dt}. \tag{29}$$

$I_{\text{ref\_con}}$ denotes the current reference value of converter with inertia emulation, and $I_{\text{ref\_con}} = I_{\text{ine}} + I_{\text{ref}}$.

According to Fig. 22, the real-time and accuracy of grid frequency measurement is very crucial. For the strong grid, the PLL can quickly track the grid frequency, and good effect of inertia emulation can be attained by the modified vector control. However, when the grid is weak, the PLL may induce the instability due to large bandwidth. Thus, there is a tradeoff between speed and stability of frequency detection. On the contrary, there is no PLL-induced instability in the VSG system.

For the modified vector control, the system stability is greatly influenced by the number of paralleled converters [9]. However, the parallel number of VSGs does not influence the stability of the system. Thus, from the perspective of stability, the authors therein suggest that VSG control is more preferable than the modified vector control for achieving high penetration of renewable energy generation in a weak grid.

Furthermore, the modified vector control system is equivalent to a current source. Thus, it cannot provide independent voltage support. On the contrary, the VSG system is equivalent to a voltage source, and it can work independently in the island mode.

B. Power Decoupling for High X/R

According to the typical line parameters in Table V [42], when the voltage level is high, the X/R is relatively large. Note that

TABLE V
TYPICAL LINE PARAMETERS

Type of line	$R(\Omega/km)$	$X(\Omega/km)$	R/X
Low Voltage	0.64	0.08	7.70
Medium Voltage	0.16	0.19	0.85
High Voltage	0.06	0.19	0.31

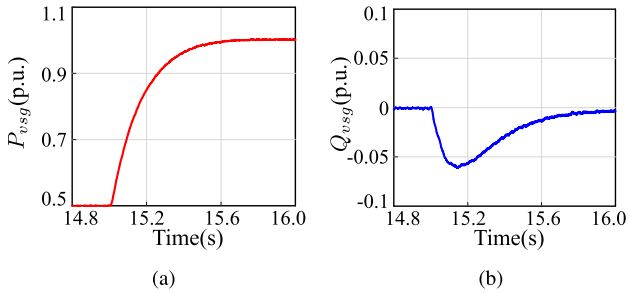

Fig. 23. Simulation results of P_{vsg} and Q_{vsg} for $\zeta_v = 0.10$ when $r_g = 0.1$ p.u. and $x_g = 0.4$ p.u. (a) P_{vsg}. (b) Q_{vsg}.

the core idea of this article is to ensure sufficient voltage output range. In addition, when X/R is larger than the theoretical value, the output voltage is relatively high, and negative compensation is needed in this situation. Thus, combined with the analysis in Section IV, to ensure sufficient voltage output range of the GCC, (19) should be changed to

$$v_{cd} = V_c' - \zeta_v i_{od}, \quad v_{cq} = 0. \tag{30}$$

Similar to the calculation in Section IV-B, the final small-signal model can be attained accordingly. For $r_g = 0.1$ p.u. and $x_g = 0.4$ p.u., when P_{vsg} changes from 0.5 to 1.0 p.u., the ideal ζ_v is about 0.10. To verify the rationality of theoretical analysis, the simulation results of P_{vsg} and Q_{vsg} are shown in Fig. 23. Apparently, when $\zeta_v = 0.1$ p.u., power coupling can be eliminated. Thus, the decoupling ideas and analysis in this article can also solve the coupling issue with high X/R ratio.

Apparently, the information of X/R is needed to quantitatively design the needed voltage compensation. When the parameter deviation is within a certain range, the proposed method is effective. For example, if the measured X/R is smaller than the actual value, larger voltage compensation will be given. As a result, the VSG system will output some reactive power, which is good for the voltage support. If the measured X/R is

larger than the actual value, smaller voltage compensation will be given. Consequently, the decoupling effect is sacrificed, and the power coupling cannot be eliminated. When the parameter deviation is large, the effect of the proposed method degrades. The worst case is that the actual X/R is much smaller than the critical value [34], but the measured X/R is much larger than it. In this situation, the coupling will become worse.

VII. Conclusion

In this article, the power coupling of the VSG control is thoroughly investigated, the decoupling capability is evaluated, and the reason why coupling reduction of the virtual inductor is limited is also analyzed. Afterward, a simple QVPDC method is proposed to further reduce the power coupling. With the detailed model, the theoretical analysis indicates that the power coupling can be eliminated with the proposed method, and the power delivery capacity of the VSG can also be improved. Simulation and experiment are carried out to verify the proposed method. The main conclusions are summarized as follows.

1) The power coupling issue in the VSG system stems from the fact that voltage is not a global variable and varies across the system. The effectiveness of the decoupling strategy can be attributed to the compensation of output voltage.
2) The decoupling effect of the virtual inductor is limited by its voltage compensation capability, and this is caused by the d-axis voltage drop, which has a negative effect on the voltage compensation when x_v is relatively large.
3) The QVPDC method and the corresponding decoupling parameter design proposed in this article can eliminate the power coupling. As a result, the power delivery capacity and grid support capability of the GCC can be improved.

References

[1] J. Chen and T. O'Donnell, "Analysis of virtual synchronous generator control and its response based on transfer functions," *IET Power Electron.*, vol. 12, no. 11, pp. 2965–2977, 2019.

[2] H. Geng, X. Xi, L. Liu, G. Yang, and J. Ma, "Hybrid modulated active damping control for DFIG-based wind farm participating in frequency response," *IEEE Trans. Energy Convers.*, vol. 32, no. 3, pp. 1220–1230, Sep. 2017.

[3] P. Veers *et al.*, "Grand challenges in the science of wind energy," *Science*, vol. 366, no. 6464, 2019, Art. no. eaau2027.

[4] F. Blaabjerg, R. Teodorescu, M. Liserre, and A. V. Timbus, "Overview of control and grid synchronization for distributed power generation systems," *IEEE Trans. Ind. Electron.*, vol. 53, no. 5, pp. 1398–1409, Oct. 2006.

[5] M. F. Arani and Y. A.-R. I. Mohamed, "Analysis and impacts of implementing droop control in DFIG-based wind turbines on microgrid/weak-grid stability," *IEEE Trans. Power Syst.*, vol. 30, no. 1, pp. 385–396, Jan. 2015.

[6] H.-P. Beck and R. Hesse, "Virtual synchronous machine," in *Proc. 9th Int. Conf. Elect. Power Qual. Utilisation*, Barcelona, Spain, 2007, pp. 1–6.

[7] S. Zhou *et al.*, "An improved design of current controller for LCL-type grid-connected converter to reduce negative effect of PLL in weak grid," *IEEE J. Emerg. Sel. Topics Power Electron.*, vol. 6, no. 2, pp. 648–663, Jun. 2018.

[8] D. Zhu, S. Zhou, X. Zou, and Y. Kang, "Improved design of PLL controller for LCL-type grid-connected converter in weak grid," *IEEE Trans. Power Electron.*, vol. 35, no. 5, pp. 4715–4727, May 2020.

[9] W. Wu *et al.*, "Sequence-impedance-based stability comparison between VSGs and traditional grid-connected inverters," *IEEE Trans. Power Electron.*, vol. 34, no. 1, pp. 46–52, Jan. 2019.

[10] H. Li, X. Zhang, T. Shao, and T. Q. Zheng, "Flexible inertia optimization for single-phase voltage source inverter based on hold filter," *IEEE J. Emerg. Sel. Topics Power Electron.*, vol. 7, no. 2, pp. 1300–1310, Jun. 2019.

[11] H. Wu *et al.*, "Small-signal modeling and parameters design for virtual synchronous generators," *IEEE Trans. Ind. Electron.*, vol. 63, no. 7, pp. 4292–4303, Jul. 2016.

[12] A. Karimi *et al.*, "Inertia response improvement in AC microgrids: A fuzzy-based virtual synchronous generator control," *IEEE Trans. Power Electron.*, vol. 35, no. 4, pp. 4321–4331, Apr. 2020.

[13] K. Jiang, H. Su, H. Lin, K. He, H. Zeng, and Y. Che, "A practical secondary frequency control strategy for virtual synchronous generator," *IEEE Trans. Smart Grid*, vol. 11, no. 3, pp. 2734–2736, May 2020.

[14] A. Asrari, M. Mustafa, M. Ansari, and J. Khazaei, "Impedance analysis of virtual synchronous generator-based vector controlled converters for weak AC grid integration," *IEEE Trans. Sustain. Energy*, vol. 10, no. 3, pp. 1481–1490, Jul. 2019.

[15] L. Huang, H. Xin, and Z. Wang, "Damping low-frequency oscillations through VSC-HVDC stations operated as virtual synchronous machines," *IEEE Trans. Power Electron.*, vol. 34, no. 6, pp. 5803–5818, Jul. 2019.

[16] G. Li *et al.*, "Analysis and mitigation of sub-synchronous resonance in series-compensated grid-connected system controlled by virtual synchronous generator," *IEEE Trans. Power Electron.*, vol. 35, no. 10, pp. 11096–11107, Oct. 2020.

[17] J. Alipoor, Y. Miura, and T. Ise, "Power system stabilization using virtual synchronous generator with alternating moment of inertia," *IEEE J. Emerg. Sel. Topics Power Electron.*, vol. 3, no. 2, pp. 451–458, Jun. 2015.

[18] M. Li, W. Huang, N. Tai, L. Yang, D. Duan, and Z. Ma, "A dual-adaptivity inertia control strategy for virtual synchronous generator," *IEEE Trans. Power Syst.*, vol. 35, no. 1, pp. 594–604, Jan. 2020.

[19] J. Liu, Y. Miura, H. Bevrani, and T. Ise, "A unified modeling method of virtual synchronous generator for multi-operation-mode analyses," *IEEE J. Emerg. Sel. Topics Power Electron.*, to be published, doi: 10.1109/JESTPE.2020.2970025.

[20] J. Jongudomkarn, J. Liu, Y. Yanagisawa, H. Bevrani, and T. Ise, "Model predictive control for indirect boost matrix converter based on virtual synchronous generator," *IEEE Access*, vol. 8, pp. 60364–60381, 2020.

[21] K. M. Cheema and K. Mehmood, "Improved virtual synchronous generator control to analyse and enhance the transient stability of microgrid," *IET Renew. Power Gener.*, vol. 14, no. 4, pp. 495–505, 2020.

[22] K. Shi, W. Song, H. Ge, P. Xu, Y. Yang, and F. Blaabjerg, "Transient analysis of microgrids with parallel synchronous generators and virtual synchronous generators," *IEEE Trans. Energy Convers.*, vol. 35, no. 1, pp. 95–105, Mar. 2020.

[23] Y. W. Li and C. Kao, "An accurate power control strategy for power-electronics-interfaced distributed generation units operating in a low-voltage multibus microgrid," *IEEE Trans. Power Electron.*, vol. 24, no. 12, pp. 2977–2988, Dec. 2009.

[24] B. Li and L. Zhou, "Power decoupling method based on the diagonal compensating matrix for VSG-controlled parallel inverters in the microgrid," *Energies*, vol. 10, no. 12, pp. 2159–2171, 2017.

[25] D. Yang, X. Wang, F. Liu, K. Xin, Y. Liu, and F. Blaabjerg, "Adaptive reactive power control of PV power plants for improved power transfer capability under ultra-weak grid conditions," *IEEE Trans. Smart Grid*, vol. 10, no. 2, pp. 1269–1279, Mar. 2019.

[26] L. Huang, H. Xin, Z. Wang, L. Zhang, K. Wu, and J. Hu, "Transient stability analysis and control design of droop-controlled voltage source converters considering current limitation," *IEEE Trans. Smart Grid*, vol. 10, no. 1, pp. 578–591, Jan. 2019.

[27] Y. Li and Y. W. Li, "Power management of inverter interfaced autonomous microgrid based on virtual frequency-voltage frame," *IEEE Trans. Smart Grid*, vol. 2, no. 1, pp. 30–40, Mar. 2011.

[28] C. N. Rowe, T. J. Summers, R. E. Betz, D. J. Cornforth, and T. G. Moore, "Arctan power-frequency droop for improved microgrid stability," *IEEE Trans. Power Electron.*, vol. 28, no. 8, pp. 3747–3759, Aug. 2013.

[29] T. Wu, Z. Liu, J. Liu, S. Wang, and Z. You, "A unified virtual power decoupling method for droop-controlled parallel inverters in microgrids," *IEEE Trans. Power Electron.*, vol. 31, no. 8, pp. 5587–5603, Aug. 2016.

[30] A. Solanki, A. Nasiri, V. Bhavaraju, Y. L. Familiant, and Q. Fu, "A new framework for microgrid management: Virtual droop control," *IEEE Trans. Smart Grid*, vol. 7, no. 2, pp. 554–566, Mar. 2016.

[31] M. Li *et al.*, "A novel virtual synchronous generator control strategy based on improved swing equation emulating and power decoupling method," in *Proc. IEEE Energy Convers. Congr. Expo.*, Milwaukee, WI, USA, 2016, pp. 1–7.

[32] S. Dong and Y. C. Chen, "Adjusting synchronverter dynamic response speed via damping correction loop," *IEEE Trans. Energy Convers.*, vol. 32, no. 2, pp. 608–619, Jun. 2017.
[33] M. Li, Y. Wang, Y. Liu, N. Xu, S. Shu, and W. Lei, "Enhanced power decoupling strategy for virtual synchronous generator," *IEEE Access*, vol. 8, pp. 73601–73613, 2020.
[34] T. Wen, X. Zou, D. Zhu, X. Guo, L. Peng, and Y. Kang, "Comprehensive perspective on virtual inductor for improved power decoupling of virtual synchronous generator control," *IET Renew. Power Gener.*, vol. 14, no. 4, pp. 485–494, 2020.
[35] J. M. Guerrero, L. G. de Vicuna, J. Matas, M. Castilla, and J. Miret, "Output impedance design of parallel-connected UPS inverters with wireless load-sharing control," *IEEE Trans. Ind. Electron.*, vol. 52, no. 4, pp. 1126–1135, Aug. 2005.
[36] L. Huang, H. Xin, and F. Döfler, "H_∞-control of grid-connected converters: Design, objectives and decentralized stability certificates," *IEEE Trans. Smart Grid*, vol. 11, no. 5, pp. 3805–3816, Sep. 2020.
[37] Z. Shuai, Y. Hu, Y. Peng, C. Tu, and Z. J. Shen, "Dynamic stability analysis of synchronverter-dominated microgrid based on bifurcation theory," *IEEE Trans. Ind. Electron.*, vol. 64, no. 9, pp. 7467–7477, Sep. 2017.
[38] R. Majumder, B. Chaudhuri, A. Ghosh, R. Majumder, G. Ledwich, and F. Zare, "Improvement of stability and load sharing in an autonomous microgrid using supplementary droop control loop," *IEEE Trans. Power Syst.*, vol. 25, no. 2, pp. 796–808, May 2010.
[39] Z. Peng, J. Wang, D. Bi, Y. Dai, and Y. Wen, "The application of microgrids based on droop control with coupling compensation and inertia," *IEEE Trans. Sustain. Energy*, vol. 9, no. 3, pp. 1157–1168, Jul. 2018.
[40] E. Bristol, "On a new measure of interaction for multivariable process control," *IEEE Trans. Autom. Control*, vol. 11, no. 1, pp. 133–134, Jan. 1966.
[41] H. Han, X.-C. Hou, J. Yang, J.-F. Wu, M. Su, and J. M. Guerrero, "Review of power sharing control strategies for islanding operation of AC microgrids," *IEEE Trans. Smart Grid*, vol. 7, no. 1, pp. 200–215, Jan. 2016.
[42] C. Li, S. K. Chaudhary, M. Savaghebi, J. C. Vasquez, and J. M. Guerrero, "Power flow analysis for low-voltage AC and DC microgrids considering droop control and virtual impedance," *IEEE Trans. Smart Grid*, vol. 8, no. 6, pp. 2754–2764, Nov. 2017.

Tiliang Wen (Student Member, IEEE) was born in Henan, China, in 1990. He received the B.Eng. degree in physics from Yangzhou University, Yangzhou, China, in 2013. He is currently working toward the Ph.D. degree with the School of Electrical and Electronic Engineering, Huazhong University of Science and Technology, Wuhan, China.

His research interests include virtual synchronous generators, stability analysis, and inertial response of renewable energy generation systems.

Donghai Zhu (Member, IEEE) was born in Anhui, China, in 1992. He received the Ph.D. degree in electrical engineering from the Huazhong University of Science and Technology, Wuhan, China, in 2018.

He is currently a Faculty Member with the School of Electrical and Electronic Engineering, Huazhong University of Science and Technology. His current research interests include the stability analysis, fault characteristics analysis, self-stabilizing control, and fault ride-through control of renewable energy generation systems.

Dr. Zhu was selected for the National Postdoctoral Program for Innovative Talents in 2018 and the Postdoctoral Post for Innovative Research in Hubei Province in 2019. He was a recipient of the *International Journal of Electrical Power and Energy Systems* Outstanding Reviewer in 2018 and the IEEE TRANSACTIONS ON ENERGY CONVERSION Best Paper Award in 2019.

Xudong Zou (Member, IEEE) was born in Hunan, China, in 1974. He received the B.S., M.S., and Ph.D. degrees in electrical engineering from the Huazhong University of Science and Technology, Wuhan, China, in 1997, 2000, and 2005, respectively.

Since 2005, he has been a Faculty Member with the Huazhong University of Science and Technology, where he is currently a Full Professor with the School of Electrical and Electronic Engineering. His current research interests include power electronic converters, renewable energy generation systems, and flywheel energy storage.

Dr. Zou was a recipient of the IEEE TRANSACTIONS ON ENERGY CONVERSION Best Paper Award in 2019.

Bingchen Jiang (Student Member, IEEE) was born in Sichuan, China, in 1995. She received the B.S. degree in electrical engineering from Chongqing University, Chongqing, China, in 2017, and the M.S. degree in clean and renewable energy from Mines ParisTech, Paris, France, in 2020. She is currently working toward the dual M.S. degree with the China-EU Institute for Clean and Renewable Energy, Huazhong University of Science and Technology, Wuhan, China.

Her research interests include renewable energy technology, advanced control methods of converters, and stability and power quality of converter-based power systems.

Li Peng (Member, IEEE) received the B.S., M.S., and Ph.D. degrees in electrical engineering from the Huazhong University of Science and Technology (HUST), Wuhan, China, in 1989, 1992, and 2004, respectively.

In 1992, she joined the HUST, where she is currently a Full Professor with the School of Electrical and Electronic Engineering. Her research interests include power electronic conversion, its control and applications, modular power supply and parallel control techniques, renewable energy generation, power quality control, and modular multilevel converters for HVdc applications.

Dr. Peng is an Associate Editor for the IEEE TRANSACTIONS ON POWER ELECTRONICS.

Yong Kang (Senior Member, IEEE) was born in Hubei, China, in 1965. He received the B.E., M.E., and Ph.D. degrees in electrical engineering from the Huazhong University of Science and Technology, Wuhan, China, in 1988, 1991, and 1994, respectively.

Since 1994, he has been a Faculty Member with the Huazhong University of Science and Technology, where he is currently a Full Professor with the School of Electrical and Electronic Engineering. His research interests include the power electronic converters, ac drivers, and renewable energy generation systems.

Dr. Kang was a recipient of the Delta Scholar Award from the Delta Environmental and Educational Foundation in 2005, and supported by the Program for New Century Excellent Talents in University from the Chinese Ministry of Education in 2004. In 2017, he was appointed as the Chief Scientist of the National Key R&D Program of China. He was a recipient of the highly prestigious China National Science and Technology Award in 2019. He is the Vice Chairman of the China UPS Standard Committee and an Associate Editor for the *Journal of Power Electronics*.